View metadata, citation and similar papers at core.ac.uk

brought to you by CORE

provided by Online Research Database In Technology

Technical University of Denmark

Micro-four-point Probe Hall effect Measurement method

Petersen, Dirch Hjorth; Hansen, Ole; Lin, Rong; Nielsen, Peter Folmer

Published in:
Journal of Applied Physics

Link to article, DOI:
10.1063/1.2949401

Publication date:
2008

Document Version
Publisher's PDF, also known as Version of record

Link back to DTU Orbit

Citation (APA):
Petersen, D. H., Hansen, O., Lin, R., & Nielsen, P. F. (2008). Micro-four-point Probe Hall effect Measurement method. Journal of Applied Physics, 104(1), 013710. DOI: 10.1063/1.2949401

DTU Library
Technical Information Center of Denmark

General rights
Copyright and moral rights for the publications made accessible in the public portal are retained by the authors and/or other copyright owners and it is a condition of accessing publications that users recognise and abide by the legal requirements associated with these rights.

- Users may download and print one copy of any publication from the public portal for the purpose of private study or research.
- You may not further distribute the material or use it for any profit-making activity or commercial gain
- You may freely distribute the URL identifying the publication in the public portal

If you believe that this document breaches copyright please contact us providing details, and we will remove access to the work immediately and investigate your claim.

Micro-four-point probe Hall effect measurement method

Dirch H. Petersen,[1,2] Ole Hansen,[1,3,a)] Rong Lin,[2] and Peter F. Nielsen[2]
[1]*Department of Micro- and Nanotechnology, Technical University of Denmark, DTU Nanotech Building 345 East, DK-2800 Kgs. Lyngby, Denmark*
[2]*CAPRES A/S, Scion-DTU, Building 373, DK-2800 Kgs. Lyngby, Denmark*
[3]*Danish National Research Foundation's Center for Individual Nanoparticle Functionality (CINF), Technical University of Denmark, Building 312, DK-2800 Kgs. Lyngby, Denmark*

(Received 18 February 2008; accepted 23 May 2008; published online 11 July 2008)

We report a new microscale Hall effect measurement method for characterization of semiconductor thin films without need for conventional Hall effect geometries and metal contact pads. We derive the electrostatic potential resulting from current flow in a conductive filamentary sheet with insulating barriers and with a magnetic field applied normal to the plane of the sheet. Based on this potential, analytical expressions for the measured four-point resistance in presence of a magnetic field are derived for several simple sample geometries. We show how the sheet resistance and Hall effect contributions may be separated using dual configuration measurements. The method differs from conventional van der Pauw measurements since the probe pins are placed in the interior of the sample region, not just on the perimeter. We experimentally verify the method by micro-four-point probe measurements on ultrashallow junctions in silicon and germanium. On a cleaved silicon ultrashallow junction sample we determine carrier mobility, sheet carrier density, and sheet resistance from micro-four-point probe measurements under various experimental conditions, and show with these conditions reproducibility within less than 1.5%. © *2008 American Institute of Physics*. [DOI: 10.1063/1.2949401]

I. INTRODUCTION

In processing of semiconductor devices a wide range of analytical techniques are applied for process control and characterization,[1] which is essential due to the very high complexity of the full process flow and due to the high costs involved. Process control and characterization will become even more important and difficult in the future due to the continued scaling of, e.g., complementary metal–oxide–semiconductor (CMOS) processes. In these CMOS processes extremely shallow (<20 nm) source/drain extensions with very high carrier concentration and high carrier mobility are required.[2] Several techniques are applied for characterization of activated ion-implanted shallow junctions; some of these require specialized sample preparation others are destructive or require delicate calibration.[1] Among the parameters that must be characterized are sheet resistance, sheet carrier density, and carrier mobility. Four-point probes are widely used for sheet resistance characterization since essentially no additional sample preparation is necessary.[1] It has recently been shown that micro-four-point probes[3] are able to accurately measure sheet resistance of ultrashallow junctions with high spatial resolution[4] and without artifacts due to probe penetration[5] and leakage current;[6] moreover carrier profiling on beveled ultrashallow junctions has been demonstrated.[7,8]

The implantation and annealing processes used in semiconductor fabrication today cannot guarantee 100% activation of the implanted dose, and defects not removed by annealing may lead to reduced carrier mobility.[9] While standard four-point probe measurements characterize the sheet resistance only, a combination with Hall effect[10] or van der Pauw[11,12] measurements allow separation of the carrier sheet density and mobility contributions to the sheet resistance. The Hall effect characterization, however, usually requires some level of sample preparation, which might even be destructive, e.g., machining of a Greek cross from the sample.[1]

In this work we show analytically and experimentally that standard micro-four-point probes can be applied to Hall effect measurements on thin films in addition to the conventional sheet resistance measurement application. The only additional requirements are that at least one lateral insulating boundary must be present on the sample and that a strong magnetic field can be applied normal to the sample surface. The theoretical findings are verified experimentally by electrical characterization of highly doped ultrashallow junctions in Si and Ge where sheet resistance, sheet carrier concentration, and Hall mobility are determined.

II. THEORY

In a four-point probe measurement a current I_0 is forced through the sample surface using two of the four probe pins, while the resulting potential difference is measured between the two remaining probe pins. The current flow in the sample results in an electrostatic potential distribution at the sample surface, $\Phi(\mathbf{r})=\Phi(\mathbf{r},\mathbf{r}_+,\mathbf{r}_-)$, which is a function of the position of interest, $\mathbf{r}$, the positions of the current injection points, $\mathbf{r}_+$ and $\mathbf{r}_-$, and the sample geometry and resistivity.

We shall consider primarily the colinear probe pin configurations B and B′, as shown in Fig. 1. In configuration B, the current is forced through the sample from pin No. 1 to pin No. 3, $\mathbf{r}_+=\mathbf{r}_1$ and $\mathbf{r}_-=\mathbf{r}_3$, while the potential difference

a)Electronic mail: oh@mk.dtu.dk.

 © 2008 American Institute of Physics

Downloaded 08 Aug 2009 to 192.38.67.112. Redistribution subject to AIP license or copyright; see http://jap.aip.org/jap/copyright.jsp

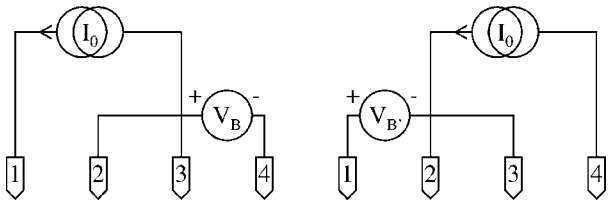

FIG. 1. The four-point probe configurations B and B′. The four probe pins (Nos. 1–4) have position vectors $\mathbf{r}_1$, $\mathbf{r}_2$, $\mathbf{r}_3$, and $\mathbf{r}_4$, respectively. In configuration B probe pins Nos. 1 and 3 are used for current injection, while probe pins Nos. 2 and 4 are used for potential measurements. In configuration B′ the role of the probe pins is reversed.

between pins Nos. 2 and 4 is measured. In configuration B′ the role of the pins is reversed. It follows, that the measured voltages in configurations B and B′ are

$$V_B = \Phi(\mathbf{r}_2,\mathbf{r}_1,\mathbf{r}_3) - \Phi(\mathbf{r}_4,\mathbf{r}_1,\mathbf{r}_3), \tag{1}$$

$$V_{B'} = \Phi(\mathbf{r}_1,\mathbf{r}_2,\mathbf{r}_4) - \Phi(\mathbf{r}_3,\mathbf{r}_2,\mathbf{r}_4), \tag{2}$$

respectively, where $\mathbf{r}_i$ is the in-plane position vector of pin No. i. In micro-four-point probe Hall effect measurements the difference, $\Delta V_{BB'} \equiv V_B - V_{B'}$, between these voltages and their average, $V_{BB'} \equiv (V_B + V_{B'})/2$, turns out to be particularly useful. In any case, the essential problem is to find the electrostatic potential $\Phi(\mathbf{r},\mathbf{r}_+,\mathbf{r}_-)$ at the surface of the sample in presence of an applied magnetic flux density.

We shall restrict the analysis to thin, laterally homogenous filamentary samples with insulating boundaries. The sample thickness h is assumed small compared to the lateral sample dimensions and to the probe pitch. We shall use Cartesian coordinates with base vectors $\mathbf{e}_x$, $\mathbf{e}_y$, and $\mathbf{e}_z$. Moreover, the magnetic flux density $\mathbf{B}$ is assumed constant and normal to the sample $\mathbf{B} = B_z\mathbf{e}_z$. As a result, the current density, $\mathbf{J}$, the electric field, $\mathbf{E}$, and the Lorentz force, $\mathbf{F} = Ze(\mathbf{E} + \mathbf{v}_d \times \mathbf{B})$, are normal to the magnetic flux density except in a small region in close proximity of the current injection points; we shall ignore this region since its effect is insignificant on a length scale set by the probe pitch. It follows that the problem of solving for the potential and the electric field is reduced to two dimensions. Here Ze is the carrier charge ($Z = \pm 1$), e the unit charge, and $\mathbf{v}_d$ is the carrier drift velocity. With these simplifications the current density becomes[13,14]

$$\mathbf{J} = \sigma_d(\mathbf{E} - Z\mu_H\mathbf{B} \times \mathbf{E}), \tag{3}$$

where we have explicitly used the condition $\mathbf{B}\cdot\mathbf{E} = 0$. σ_d is the direct conductivity and μ_H the Hall mobility, both of these parameters might be dependent on the magnetic flux density magnitude. It follows that a tensorial two-dimensional (2D) conductivity $\boldsymbol{\sigma}$ and a corresponding 2D resistivity tensor $\boldsymbol{\varrho} = \boldsymbol{\sigma}^{-1}$ can be defined[15]

$$\boldsymbol{\sigma} = \begin{pmatrix} \sigma_d & \sigma_H \\ -\sigma_H & \sigma_d \end{pmatrix},$$

$$\boldsymbol{\varrho} = \begin{pmatrix} \varrho_0 & -\varrho_H \\ \varrho_H & \varrho_0 \end{pmatrix}, \tag{4}$$

where the resistivity $\varrho_0 = [\sigma_d(1 + \mu_H^2 B_z^2)]^{-1}$, and the Hall conductivity $\sigma_H = \sigma_d Z\mu_H B_z$, while the Hall resistivity $\varrho_H = \varrho_0 Z\mu_H B_z$.

Conventionally, the Hall coefficient $\mathcal{R}_H$ is used as the primary measured entity in Hall effect measurements. The Hall coefficient $\mathcal{R}_H \equiv \mathbf{E}\cdot(\mathbf{B}\times\mathbf{J})/|\mathbf{B}\times\mathbf{J}|^2 = Z\mu_H\varrho_0 = \varrho_H/B_z$ with the conditions given here.[14] The Hall coefficient has the same sign as the carrier charge and is inversely proportional to the carrier density. Unfortunately the Hall mobility is different from the carrier conductivity mobility μ, $\mu_H = r_H\mu$, where r_H is the Hall scattering factor. The Hall scattering factor is of the order 1 and accounts for the different statistical averaging needed for the two mobilities,[14] $r_H = \langle\tau_m^2\rangle/\langle\tau_m\rangle^2$, where τ_m is the momentum relaxation time.

If the thin sample is nonhomogenous in the z direction, such that $\sigma_d = \sigma_d(z)$ and $\mu_H = \mu_H(z)$, the potential remains two dimensional, $\Phi = \Phi(x,y)$, except in the small region in close proximity of the current injection points. The current density, however, varies in the z-direction $\mathbf{J} = \mathbf{J}(x,y,z)$, while $J_z = 0$. Integration of Eq. (3) across the thickness of the sample yields the sheet current density $\mathbf{J}_S = \mathbf{J}_S(x,y)$,

$$\mathbf{J}_S \equiv \int_0^h \mathbf{J}\mathrm{d}z = \mathbf{E}\int_0^h \sigma_d \mathrm{d}z - \mathbf{e}_z \times \mathbf{E}\int_0^h \sigma_H \mathrm{d}z, \tag{5}$$

where the direct sheet conductance G_d and the Hall sheet conductance G_H can be defined as follows:

$$G_d \equiv \int_0^h \sigma_d \mathrm{d}z \quad \text{and} \quad G_H \equiv \int_0^h \sigma_H \mathrm{d}z. \tag{6}$$

With this definition Eq. (5) becomes

$$\mathbf{J}_S = G_d\mathbf{E} - G_H\mathbf{e}_z \times \mathbf{E}. \tag{7}$$

It follows that sheet conductance, $\boldsymbol{G}_S$, and sheet resistance, $\boldsymbol{R}_S = \boldsymbol{G}_S^{-1}$, tensors,

$$\boldsymbol{G}_S = \begin{pmatrix} G_d & G_H \\ -G_H & G_d \end{pmatrix},$$

$$\boldsymbol{R}_S = \begin{pmatrix} R_0 & -R_H \\ R_H & R_0 \end{pmatrix}, \tag{8}$$

may be defined, where the direct sheet resistance is $R_0 = [G_d(1 + G_H^2/G_d^2)]^{-1}$, while the relative Hall sheet resistance equals the relative Hall sheet conductance, $R_H/R_0 = G_H/G_d$. In analogy to the Hall coefficient a sheet Hall coefficient may be defined as $\mathcal{R}_{\mathrm{HS}} \equiv \mathbf{E}\cdot(\mathbf{B}\times\mathbf{J}_S)/|\mathbf{B}\times\mathbf{J}_S|^2 = R_H/B_z$.[1]

In the homogenous region of interest, Ω, the sheet current density must be divergence free, $\nabla\cdot\mathbf{J}_S = 0$, except at the current injection points, furthermore, the sheet current density normal to the insulating boundary $\delta\Omega$ must vanish. It follows from Eq. (7) that the electrostatic potential, Φ, must fulfill

$$\nabla\cdot\mathbf{J}_S = -G_d\nabla_{2\mathrm{D}}^2\Phi = I_0[\delta(\mathbf{r}-\mathbf{r}_+) - \delta(\mathbf{r}-\mathbf{r}_-)] \text{ in } \Omega,$$

Downloaded 08 Aug 2009 to 192.38.67.112. Redistribution subject to AIP license or copyright; see http://jap.aip.org/jap/copyright.jsp

$$\mathbf{J}_S \cdot \mathbf{n} = (G_d \mathbf{E} - G_H \mathbf{e}_z \times \mathbf{E}) \cdot \mathbf{n} = 0 \quad \text{on} \quad \delta\Omega, \tag{9}$$

since $\mathbf{E}=-\nabla\Phi$, and $\nabla\cdot(\mathbf{B}\times\mathbf{E})=\mathbf{E}\cdot(\nabla\times\mathbf{B})-\mathbf{B}\cdot(\nabla\times\mathbf{E})=0$ for a constant position- and time-independent magnetic flux density. Here $\mathbf{r}=(x,y)$ is the in-plane position vector, $\mathbf{r}_+$ and $\mathbf{r}_-$ are the points where the currents $\pm I_0$ are injected, while $\mathbf{n}$ is the unit vector normal to the lateral insulating boundary $\delta\Omega$, and $\delta(\mathbf{r})$ is Dirac's delta function. Note the magnetic flux density affects the potential only through the boundary conditions.

In Secs. II A–II C and in the Appendix, we shall solve Eq. (9) for a number of sample geometries relevant to four-point probe measurements; these solutions differ from the solutions given by van der Pauw[12] since the probe pins are assumed to be in the interior of the region Ω, and not restricted to the perimeter $\delta\Omega$ as assumed by van der Pauw.

A. Infinite sheet

If the lateral boundaries of the sample are infinitely far from the current injection points the potential which solves Eq. (9) is particularly simple, a superposition of two logarithmic potentials

$$\Phi(\mathbf{r}) = \frac{I_0}{2\pi G_d} \ln\frac{|\mathbf{r}-\mathbf{r}_-|}{|\mathbf{r}-\mathbf{r}_+|} = \frac{I_0 R_0}{2\pi}\left(1+\frac{R_H^2}{R_0^2}\right)\ln\frac{|\mathbf{r}-\mathbf{r}_-|}{|\mathbf{r}-\mathbf{r}_+|}, \tag{10}$$

which is formally identical to the solution[16] for zero magnetic flux density except for the effect of the magnetic flux density on the direct conductivity, $\sigma_d=\sigma_d(B)$. The current density, however, is different since it is not only a sum of two purely radial current density contributions, two additional tangential current density contributions around each current injection point are also needed.

Using the colinear probe configurations B and B′, as shown in Fig. 1, we find from the potential in Eq. (10) that the measured voltages V_B and $V_{B'}$ are equal

$$V_B = V_{B'} = \frac{I_0 R_0}{2\pi}\left(1+\frac{R_H^2}{R_0^2}\right)\ln\frac{|\mathbf{r}_2-\mathbf{r}_3|\,|\mathbf{r}_4-\mathbf{r}_1|}{|\mathbf{r}_2-\mathbf{r}_1|\,|\mathbf{r}_4-\mathbf{r}_3|}, \tag{11}$$

a result that is valid for an arbitrary two-dimensional spatial arrangement of the four probe pins. If the probe pins are equidistant with the pitch s, the measured voltages in the two configurations are

$$V_B = V_{B'} = \frac{I_0 R_0}{2\pi}\left(1+\frac{R_H^2}{R_0^2}\right)\ln 3, \tag{12}$$

a result that except for the factor $(1+R_H^2/R_0^2)=(1+\bar{\mu}_H^2 B_z^2)$ is identical to the result at zero magnetic flux density. This factor accounts for part of the magnetoresistance, which at ordinary magnetic flux densities is a quite small effect, except in very high mobility samples. The average Hall mobility $\bar{\mu}_H$ is defined in Eq. (24).

B. Semi-infinite sheet—Upper half-plane

In the case of the semi-infinite sheet, $y\geq 0$, the solution to Eq. (9) can be obtained using the method of images;[17] the arrangement of current injection sources and images is shown in Fig. 2. The images, however, must be modified in order to fulfill the boundary condition $J_{Sy}(x,0)=0$, since the usual image method would ensure $E_y(x,0)=0$, while $J_{Sy}(x,0)=0$ requires $G_d E_y(x,0)-G_H E_x(x,0)=0$ and thus $E_y(x,0)=(G_H/G_d)E_x(x,0)$.

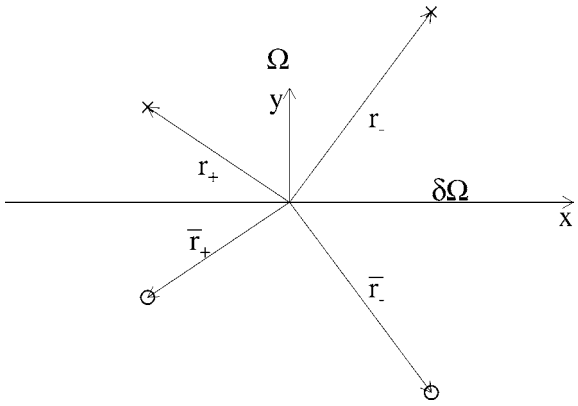

FIG. 2. The arrangement of current injection sources (×) and modified images (◯) in the case of an insulating boundary at $y=0$.

The potential that solves Eq. (9) in Ω is

$$\Phi(\mathbf{r}) = \mathcal{A}_+ \ln\frac{|\mathbf{r}-\mathbf{r}_-|}{|\mathbf{r}-\mathbf{r}_+|} + \mathcal{A}_- \ln\frac{|\mathbf{r}-\bar{\mathbf{r}}_-|}{|\mathbf{r}-\bar{\mathbf{r}}_+|} + \frac{I_0 R_H}{\pi}\left(\arctan\frac{x-x_+}{y+y_+} - \arctan\frac{x-x_-}{y+y_-}\right), \tag{13}$$

where $\bar{\mathbf{r}}_\pm=(\bar{x}_\pm,\bar{y}_\pm)=(x_\pm,-y_\pm)$ are the positions of the modified images of the sources at positions $\mathbf{r}_\pm$. The first term is the source term, while the two remaining terms originate from the images, they are thus due to the boundary conditions at $y=0$. For each of the current sources the boundary conditions are fulfilled by combining a source term representing a purely radial electric field with image terms representing a purely radial current density. For later convenience the coefficients $\mathcal{A}_+$ and $\mathcal{A}_-$ have been defined as follows:

$$\mathcal{A}_+ \equiv \frac{I_0 R_0}{2\pi}\left(1+\frac{R_H^2}{R_0^2}\right),$$

$$\mathcal{A}_- \equiv \frac{I_0 R_0}{2\pi}\left(1-\frac{R_H^2}{R_0^2}\right). \tag{14}$$

Using Eqs. (1) and (2) the measured voltages in probe configurations B and B′ are calculated (the overbar in, e.g., $\bar{\mathbf{r}}_+$ is used as an operator). From these the voltage difference $\Delta V_{BB'}$ results

$$\Delta V_{BB'} = \frac{2 I_0 R_H}{\pi}\left(\arctan\frac{x_2-x_1}{y_2+y_1} + \arctan\frac{x_3-x_2}{y_3+y_2} + \arctan\frac{x_4-x_3}{y_4+y_3} - \arctan\frac{x_4-x_1}{y_1+y_4}\right), \tag{15}$$

while the average voltage $\overline{V_{BB'}}$ becomes

Downloaded 08 Aug 2009 to 192.38.67.112. Redistribution subject to AIP license or copyright; see http://jap.aip.org/jap/copyright.jsp

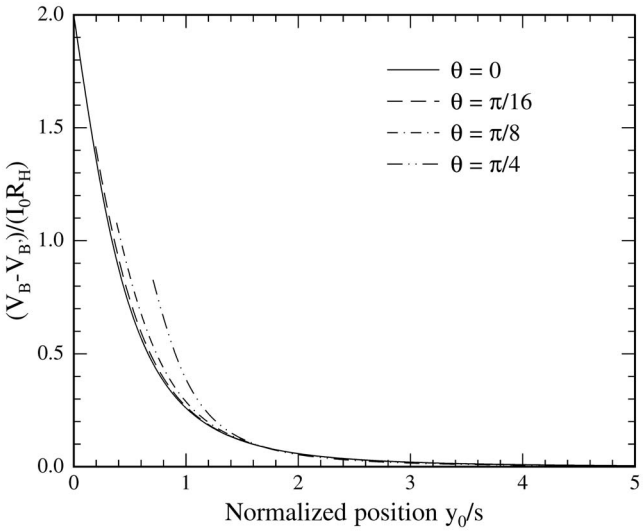

FIG. 3. The difference between measured voltages in configurations B and B′, when the region of interest is the upper half-plane, as a function of normalized position y_0/s, where y_0 is the distance from the boundary to the probe center. Calculations [Eqs. (15) and (17)] are shown for four different angles, $\theta \in [0, \pi/16, \pi/8, \pi/4]$, between the line of the probe pins and the insulating boundary; the line of the probe pins and the boundary are parallel at $\theta=0$.

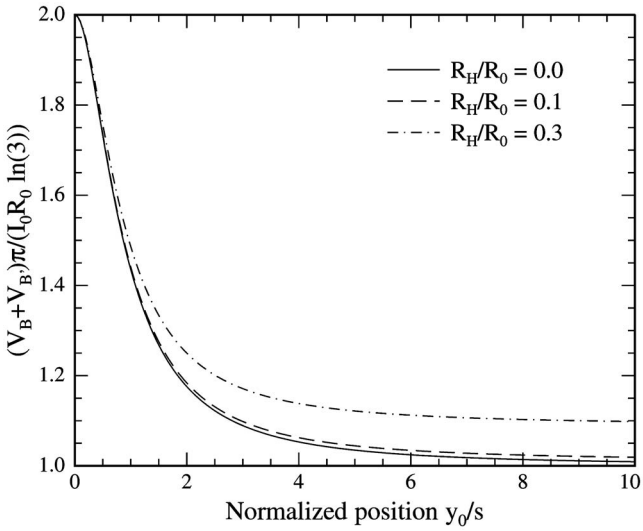

FIG. 4. Position dependence of the average of the measured voltages in configurations B and B′ when the region of interest is the upper half-plane. Voltages calculated from Eq. (18) for three different values of the relative Hall sheet resistance R_H/R_0=0.0, 0.1, and 0.3, respectively, are shown. In silicon or germanium $R_H/R_0<0.1$ at ordinary magnetic flux densities.

$$\overline{V_{BB'}} = \frac{I_0 R_0}{2\pi}\left(1+\frac{R_H^2}{R_0^2}\right)\ln\frac{|\mathbf{r}_2-\mathbf{r}_3|}{|\mathbf{r}_2-\mathbf{r}_1|}\frac{|\mathbf{r}_4-\mathbf{r}_1|}{|\mathbf{r}_4-\mathbf{r}_3|} + \frac{I_0 R_0}{2\pi}\left(1-\frac{R_H^2}{R_0^2}\right)\ln\frac{|\mathbf{r}_2-\bar{\mathbf{r}}_3|}{|\mathbf{r}_2-\bar{\mathbf{r}}_1|}\frac{|\mathbf{r}_4-\bar{\mathbf{r}}_1|}{|\mathbf{r}_4-\bar{\mathbf{r}}_3|}. \quad (16)$$

These equations are valid for any arbitrary spatial probe pin arrangement.

In a practical measurement, with equidistant, colinear four-point probe pins aligned parallel to the y axis such that the four probe pins are positioned at (is, y_0), $i \in \{0,1,2,3\}$, arranged in configurations B and B′, the measured voltages V_B and $V_{B'}$ can be combined as follows:

$$\Delta V_{BB'} = \frac{2I_0 R_H}{\pi}\left(3\arctan\frac{s}{2y_0} - \arctan\frac{3s}{2y_0}\right) \quad (17)$$

and

$$\overline{V_{BB'}} = \mathcal{A}_+ \ln 3 + \mathcal{A}_- \ln\sqrt{\frac{9+4\left(\frac{y_0}{s}\right)^2}{1+4\left(\frac{y_0}{s}\right)^2}}. \quad (18)$$

From Eq. (17) the Hall sheet resistance R_H can be extracted using measured data as a function of distance to the boundary, thereafter the direct sheet resistance R_0 can be determined using Eq. (18).

In Fig. 3, $(V_B-V_{B'})/(I_0R_H)$, calculated from Eqs. (17) and (15), is shown as a function of the normalized distance y_0/s of the probe center to the boundary at $y=0$, where $V_B-V_{B'}=2I_0R_H$. Calculations for four different angles, $\theta \in [0, \pi/16, \pi/8, \pi/4]$, between the line of probe pins and the boundary are shown; at the angle $\theta=\pi/2$ the Hall voltage contribution vanishes, $\Delta V_{BB'}=0$. The measured voltage difference is seen to be significant only very close to the boundary and vanish if the distance is more than a few times the probe pitch. The effect of a small angular misalignment between the probe and the boundary is seen to be very small in the case where parallel probe and boundary is wanted.

In Fig. 4, $(V_B+V_{B'})\pi/(I_0R_0 \ln 3)$, calculated from Eq. (18) is shown as a function of the normalized distance y_0/s from the boundary $y=0$ at three values of the relative Hall resistance, R_H/R_0. The sum of the measured voltages is independent on the relative Hall resistance close to the boundary, where the measured value, $V_B+V_{B'}=(R_0I_0 \ln 3)/\pi$, is twice the value measured very far from the edge at zero magnetic flux density. Far from the edge the full effect of the magnetoresistance affects the sum of the measured voltages. Equation (18) is reminiscent of the usual single insulating boundary proximity correction for four-point probe sheet resistance measurements on thin films.[18,19]

C. Narrow stripe

The potential in the stripe $0 \le y \le w$ with insulating boundaries at $y=0$ and $y=w$ can be found from an infinite sum of alternating modified and ordinary images. The sources and ordinary images are positioned at $\mathbf{r}_\pm + 2n\mathbf{w}$, where the vector $\mathbf{w}=w\mathbf{e}_y$ and n is an arbitrary integer, while the modified images are positioned at $\bar{\mathbf{r}}_\pm + 2n\mathbf{w}$, as illustrated in Fig. 5.

The potential that solves Eq. (9) in Ω is

$$\Phi(\mathbf{r}) = \mathcal{A}_+\sum_{n=-\infty}^{\infty}\ln\frac{|\mathbf{r}-\mathbf{r}_- - 2n\mathbf{w}|}{|\mathbf{r}-\mathbf{r}_+ - 2n\mathbf{w}|} + \mathcal{A}_-\sum_{n=-\infty}^{\infty}\ln\frac{|\mathbf{r}-\bar{\mathbf{r}}_- - 2n\mathbf{w}|}{|\mathbf{r}-\bar{\mathbf{r}}_+ - 2n\mathbf{w}|} + \frac{I_0R_H}{\pi}\sum_{n=-\infty}^{\infty}\left(\arctan\frac{x-x_+}{y+y_+-2nw} - \arctan\frac{x-x_-}{y+y_--2nw}\right). \quad (19)$$

Downloaded 08 Aug 2009 to 192.38.67.112. Redistribution subject to AIP license or copyright; see http://jap.aip.org/jap/copyright.jsp

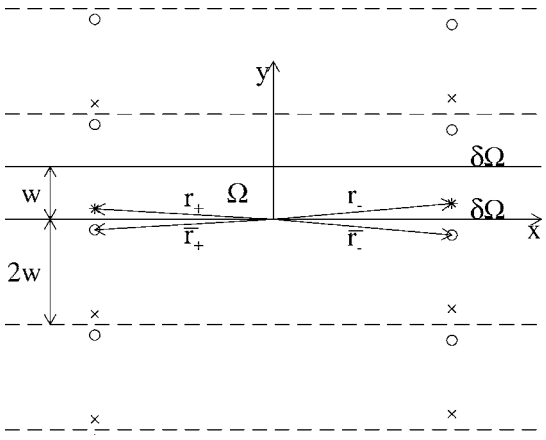

FIG. 5. Arrangement of sources (*), ordinary images (×), and modified images (◯) in the narrow stripe $0 \le y \le w$.

From this potential, the measured voltages, V_B and $V_{B'}$, in configuration B and B′ can be calculated using Eqs. (1) and (2); these voltages can be subtracted or added to yield

$$\Delta V_{BB'} = \frac{2I_0R_H}{\pi}\sum_{n=-\infty}^{\infty}\left(\arctan\frac{x_2-x_1}{y_2+y_1-2nw} + \arctan\frac{x_3-x_2}{y_3+y_2-2nw} + \arctan\frac{x_4-x_3}{y_4+y_3-2nw} - \arctan\frac{x_4-x_1}{y_4+y_1-2nw}\right), \tag{20}$$

and

$$\overline{V_{BB'}} = \mathcal{A}_+\sum_{n=-\infty}^{\infty}\ln\frac{|\mathbf{r}_2-\mathbf{r}_3-2n\mathbf{w}|\,|\mathbf{r}_4-\mathbf{r}_1-2n\mathbf{w}|}{|\mathbf{r}_2-\mathbf{r}_1-2n\mathbf{w}|\,|\mathbf{r}_4-\mathbf{r}_3-2n\mathbf{w}|} + \mathcal{A}_-\sum_{n=-\infty}^{\infty}\ln\frac{|\mathbf{r}_2-\bar{\mathbf{r}}_3-2n\mathbf{w}|\,|\mathbf{r}_4-\bar{\mathbf{r}}_1-2n\mathbf{w}|}{|\mathbf{r}_2-\bar{\mathbf{r}}_1-2n\mathbf{w}|\,|\mathbf{r}_4-\bar{\mathbf{r}}_3-2n\mathbf{w}|}. \tag{21}$$

In a practical measurement, with an equidistant, colinear four-point probe aligned parallel to the y axis such that the four probe pins are positioned at (is, y_0), $i \in \{0,1,2,3\}$, arranged in configurations B and B′, the measured voltages, V_B and $V_{B'}$, can be combined as follows:

$$\Delta V_{BB'} = \frac{2I_0R_H}{\pi}\sum_{n=-\infty}^{\infty}\left(3\arctan\frac{s}{2y_0-2nw} - \arctan\frac{3s}{2y_0-2nw}\right), \tag{22}$$

and

$$\overline{V_{BB'}} = \mathcal{A}_+\sum_{n=-\infty}^{\infty}\ln\sqrt{\frac{9s^2+4n^2w^2}{s^2+4n^2w^2}} + \mathcal{A}_-\sum_{n=-\infty}^{\infty}\ln\sqrt{\frac{9s^2+4(y_0-nw)^2}{s^2+4(y_0-nw)^2}}. \tag{23}$$

In Fig. 6, $(V_B-V_{B'})/(I_0R_H)$, calculated from Eq. (22) is shown as a function of the normalized distance y_0/s from the boundary $y=0$ for a stripe of width $w=5s$; the measured voltage difference is seen to be significant only very close to the boundaries and vanish if the distance from each boundary is more than a few times the probe pitch. In Fig. 6, the result for a half-plane, Eq. (17), is also shown for comparison; this simple result is quite similar to the result for the stripe close to the left boundary. Finally, the approximation resulting from the first two terms in Eq. (22) is shown, but cannot be distinguished from the exact solution; it follows that the sum in Eq. (22) converges very rapidly.

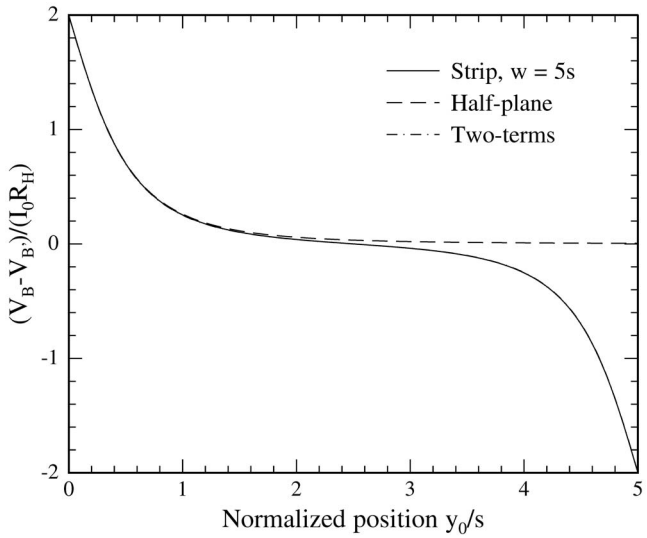

FIG. 6. Position dependence of the difference between measured voltages in configuration B and B′ when the region of interest is the stripe $0 \le y \le w$ [Eq. (22); full line]. The width of the region is assumed to be $w=5s$, where s is the probe pitch. For comparison the result for the upper half-plane region [Eq. (17); dashed line] is also shown. Finally, the approximate result from using only the first two terms in the infinite sum of Eq. (22) is shown, but cannot be distinguished from the full solution.

In Fig. 7, $(V_B+V_{B'})\pi/(I_0R_0 \ln 3)$, calculated from Eq. (23), is shown as a function of the normalized distance y_0/s

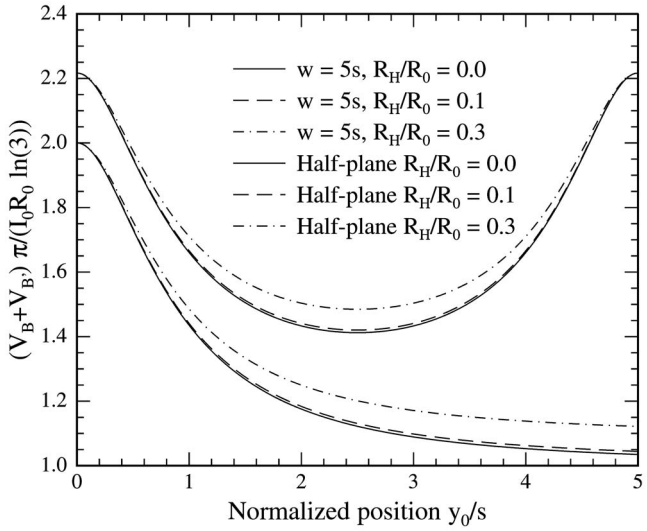

FIG. 7. Position dependence of the average measured voltages in configuration B and B′ when the region of interest is the stripe $0 \le y \le w$ [Eq. (23); upper set of curves]. The width of the region is assumed to be $w=5s$, where s is the probe pitch. For comparison results for the upper half-plane region are also shown [Eq. (18); lower set of curves]. Results for three different values of the relative Hall sheet resistance R_H/R_0 are shown.

Downloaded 08 Aug 2009 to 192.38.67.112. Redistribution subject to AIP license or copyright; see http://jap.aip.org/jap/copyright.jsp

from the boundary $y=0$ for a stripe of width $w=5s$ at three values of the relative Hall sheet resistance R_H/R_0. The sum of the measured voltages is independent on the relative Hall sheet resistance close to the boundary. Far from the edge the full effect of the magnetoresistance affects the sum of the measured voltages. The finite width of the stripe affects the sum of the measured voltages at all positions as seen from a comparison with the result for a half-plane, Eq. (18), which is also shown in Fig. 7 for convenience.

D. Interpretation of Hall effect measurements

The primary applications of Hall effect measurements on semiconductor samples are experimental characterization of Hall mobility and carrier concentration. For a homogenous sample, the Hall mobility can be calculated from the measured quantities, the Hall conductivity σ_H, the direct conductivity σ_d (or the respective resistivities), and the magnetic flux density, since $\mu_H=\sigma_H/(\sigma_d ZB_z)=\varrho_H/(\varrho_0 ZB_z)$. The Hall mobility can also be calculated from the Hall coefficient $\mu_H=\mathcal{R}_H/(\varrho_0 Z)$. For a sample with carrier density, $n=n(z)$, and thus mobility variations in the z direction a mean Hall mobility, $\bar{\mu}_H$, can be calculated from the measured Hall sheet conductance, G_H, and direct sheet conductance, G_d, according to[20]

$$\bar{\mu}_H=\frac{G_H}{G_d ZB_z}=\frac{\int_0^h n\mu\mu_H \mathrm{d}z}{\int_0^h n\mu \mathrm{d}z}=\frac{R_H}{R_0 ZB_z}, \tag{24}$$

where Eq. (6) and $\sigma_d=e\mu n$ have been used. The equation $\sigma_d=e\mu n$ is valid at sufficiently low magnetic flux densities.

For a homogenous sample the carrier density is then $n=\sigma_d/e\mu=r_H\sigma_d/(e\mu_H)=r_H ZB_z\sigma_d^2/(e\sigma_H)$. Using relations between resistivities and conductivities the carrier density becomes $n=r_H ZB_z\sigma_d\varrho_0/(e\varrho_H)\simeq r_H ZB_z/(e\varrho_H)=r_H Z/(e\mathcal{R}_H)$ and is thus easily calculated from the measured Hall resistivity if the Hall scattering factor is known. The approximation is valid at sufficiently low magnetic flux densities, where $\varrho_0 \simeq 1/\sigma_d$. For a sample that is nonhomogenous in the z direction the sheet carrier density, $N_S\equiv\int_0^h n\mathrm{d}z$, may be calculated from the measured Hall sheet resistance,[20]

$$N_S=\bar{r}_H\frac{ZB_z G_d^2}{eG_H}=\bar{r}_\mathrm{H}\frac{\left(\int_0^h n\mu\ \mathrm{d}z\right)^2}{\int_0^h n\mu\mu_H\ \mathrm{d}z}\simeq\frac{\bar{r}_H ZB_z}{eR_H}, \tag{25}$$

where the average Hall scattering factor, $\bar{r}_H$, is defined as follows:

$$\bar{r}_H=\frac{\left(\int_0^h n\mu^2 r_H \mathrm{d}z\right)\left(\int_0^h n\mathrm{d}z\right)}{\left(\int_0^h n\mu\mathrm{d}z\right)^2}. \tag{26}$$

Since much of the difficulty in interpretation of Hall measurements is related to the average Hall scattering factor, it is often conveniently assumed to equal 1 in practical Hall effect experiments. In such cases, the measured Hall mobility is still correct, but the sheet carrier density should really be stated as a Hall sheet carrier density $N_\mathrm{HS}\equiv N_S/\bar{r}_H$.

The treatment given here only apply to samples that are homogenous in the $x-y$ plane; a nonhomogenous sample is a far more difficult problem.[21]

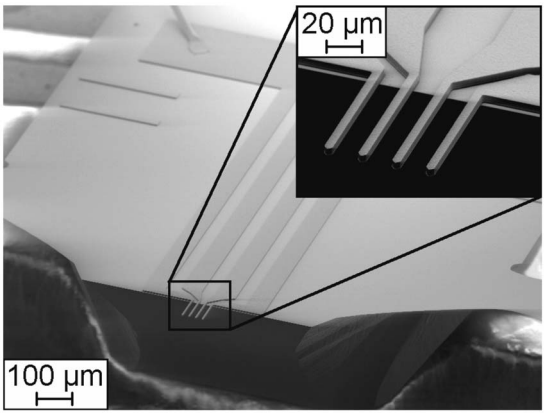

FIG. 8. SEM image of a 20 μm pitch M4PP. The 5 μm thick polysilicon cantilevers are coated with a 200 nm Ni thin film on a 10 nm Ti adhesion layer. The inset shows a close up SEM image of the cantilevers.

III. EXPERIMENTS

Microscale Hall effect measurements were performed with a micro-four-point probe (M4PP) using a CAPRES microRSP-M150 (Ref. 22) system. The M4PP used in these experiments consists of metal coated silicon cantilever electrodes extending from the edge of a silicon die; Fig. 8 shows a scanning electron microscope (SEM) image of a M4PP die with a close up image of the probe cantilevers shown in the inset. In the experiments Ni coated as well as Au coated M4PP's were used. For the microscale Hall measurements, the sample chuck of the microRSP-M150 was fitted with a permanent magnet. The resulting magnetic flux density at the position of the sample was $B_z=0.5$ T as measured using a calibrated Hall sensor.

To explore the potential of the new microscale Hall effect method, highly doped p-type silicon and p-type germanium samples with single and double insulating barrier geometry, respectively, were characterized. These samples are particularly challenging to characterize due to the rather low mobilities and therefore small relative Hall sheet resistances.

First, the sheet resistance is measured far from the insulating barrier (more than three times the electrode pitch) using dual configuration position correction.[4] This is done to determine the sheet resistance more accurately; dual configuration measurements typically allow for sheet resistance repeatability with a standard deviation on the order of 0.1%, whereas the relative standard deviation of a single configuration measurement is an order of magnitude higher depending on the electrode pitch.[23]

Then the M4PP is aligned parallel to an insulating boundary, i.e., the tips of the electrodes are positioned at (is, y_0), $i\in\{0,1,2,3\}$, while the insulating boundary is situated at $y=y_{00}$. After optical alignment, the probe is repeat-

Downloaded 08 Aug 2009 to 192.38.67.112. Redistribution subject to AIP license or copyright; see http://jap.aip.org/jap/copyright.jsp

edly engaged with the surface and moved to a new position in a direction perpendicular to the insulating boundary. During each engage, a series of four-point resistance measurements in configurations B and B′ are performed using a measurement current set-point of $I_0=100\ \mu$A. The measurement noise on $\Delta V_{BB'}=\langle V_B-V_{B'}\rangle$ is reduced by averaging the measurements during each engage.

Finally, the Hall sheet resistance R_H and the exact boundary position y_{00} in the probe coordinate system are estimated by fitting to the measured data the appropriate analytical model for the specific geometry, Eqs. (17) or (22), using a nonlinear fitting algorithm.[24] Thereafter, the Hall sheet resistance R_H and standard deviation ΔR_H is calculated using a linear regression where the positions y_0 and y_{00} are used with the analytical model to calculate a nonlinear position axis where a linear relation to $\Delta V_{BB'}$ is expected.

IV. RESULTS AND DISCUSSION

In the Secs. IV A and IV B, where measurements on ultrashallow junctions in silicon and germanium are reported, we experimentally verify the the microscale Hall effect method. A comparative experimental study of this method and alternative characterization methods on ultrashallow junctions is in progress.

A. Silicon—Single barrier

An ultrashallow junction was formed in an *n*-type (100) silicon wafer by low energy boron implantation (3 keV, 1×10^{15} cm^{-2}) followed by rapid thermal annealing (RTA). The nonpatterned wafer was cleaved to provide a well-defined straight insulating boundary. The dual configuration sheet resistance measured on the sample was $267.1\pm0.8\ \Omega$, where the uncertainty is mainly due to sample nonhomogeneity.

On this sample microscale Hall effect measurements were performed under various experimental conditions. For this sample the Hall resistance measurement data were filtered through a simple 40% median filter to eliminate severe measurement outliers (each probe position treated separately) prior to averaging. This was necessary due to measurement noise, probably related to the electrode-sample contact properties.

Figure 9 shows Hall effect measurement data (●) using a 30 μm pitch Au coated M4PP; the full line shows the model fit to the measured data, corresponding to a Hall sheet resistance, $R_H=0.562\pm0.005\ \Omega$, and the estimated boundary position, $y_{00}=0.22\ \mu$m. Hall effect measurements were done using both Au and Ni coated M4PP's in order to investigate if application of a ferromagnetic electrode metal would affect the measurement. Likewise, the effect of electrode pitch and measurement frequency was investigated by performing measurements also using a 10 μm pitch M4PP and by measurements at 11 Hz as well as 987 Hz. The Hall sheet resistances and the corresponding standard deviations extracted from model fits to measurement data are summarized in Table I, where no significant effect of the various experimental conditions is seen. The repeatability even with significant alterations of the experimental conditions is very good, the relative standard deviation on the average of the measurements in Table I is less than 1.5%. The minimum number of measurement points necessary for an accurate extraction of the Hall sheet resistance has not been investigated, but a trade-off between precision and measurement time exists; the total data acquisition time used to produce the data in Fig. 9 was 5 min.

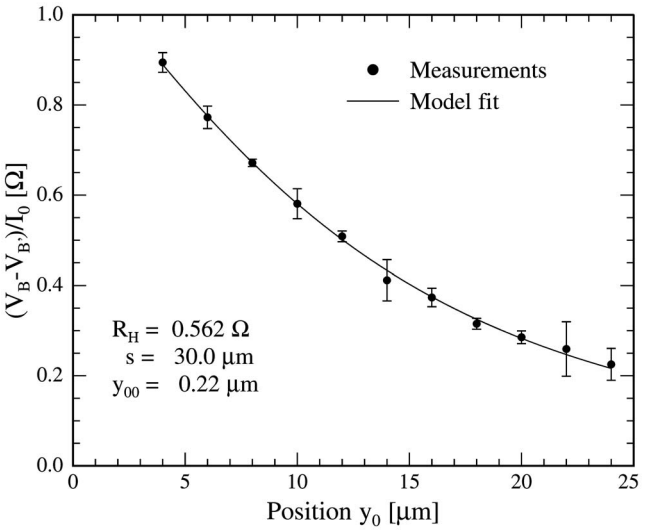

FIG. 9. Microscale Hall effect measurements on a boron doped ultrashallow junction in silicon. The silicon sample has been cleaved to form a semi-infinite sheet and a measurement scan from this edge was performed. The measurement data (●) and a fit (full line) using Eq. (17) with the Hall resistance R_H and the position of the sample edge y_{00} as fitting parameters are shown. The estimated position of the edge is $y_{00}=0.22\ \mu$m.

From the measured Hall sheet resistance and sheet resistance of the sample both active Hall sheet carrier density, N_{HS}, and average Hall mobility, $\bar{\mu}_H$, were calculated using Eqs. (24) and (25), however, since the effective Hall scattering factor is not known $\bar{r}_H=1$ is assumed. The results are summarized in Table I. The calculated active dose is approximately half of the implanted dose; this is in agreement with the expected value since the boron concentration is above the solid solubility and partial dose activation therefore expected. Finally, the Hall mobility is within 10% of the Hall mobility reported by Sasaki for highly boron doped silicon.[25]

B. Germanium—Double barrier

Microscale Hall effect measurements were also performed on a patterned shallow *p*-type junction (80 nm) formed in Ge using RTA of a boron implant (10 keV, 2×10^{15} cm^{-2}) following a preamorphization implant. The pattern used for the measurements was a double insulating barrier with a nominal distance between barriers of 100 μm. Figure 10 illustrates the measurement setup. In the measurements a 20 μm pitch M4PP probe was used at a measurement frequency of 11 Hz. For this sample data were not filtered. Figure 11 shows the measured Hall resistance data (●) resulting from a line scan across the *p*-type stripe; the full line shows a model fit—using Eq. (22)—to measured data with the Hall sheet resistance, R_H, the position of the left boundary, y_{00}, and the width of the stripe, w, as fitting parameters.

Downloaded 08 Aug 2009 to 192.38.67.112. Redistribution subject to AIP license or copyright; see http://jap.aip.org/jap/copyright.jsp

TABLE I. Hall sheet resistance R_H and standard deviation extracted from M4PP Hall effect measurements on an ultrashallow boron doped junction in silicon. The active Hall sheet carrier density N_{HS} and Hall mobility $\bar{\mu}_H$ are calculated from M4PP Hall effect and sheet resistance measurements using Eqs. (25) and (24). Four different experimental conditions with variation of electrode material (Au or Ni), probe pitch, s, and measurement frequency, f, were used.

	s (μm)	f (Hz)	$R_H \pm \Delta R_H$ (Ω)	$N_{\mathrm{HS}} \pm \Delta N_{\mathrm{HS}}$ ($\times 10^{14}$ cm^{-2})	$\bar{\mu}_H \pm \Delta \bar{\mu}_H$ (cm^2 V^{-1} s^{-1})
Au	30	11	0.562 ± 0.005	5.55 ± 0.05	42.1 ± 0.4
Ni	10	11	0.570 ± 0.015	5.48 ± 0.14	42.7 ± 1.1
Ni	30	11	0.556 ± 0.008	5.61 ± 0.08	41.6 ± 0.6
Ni	30	987	0.551 ± 0.003	5.66 ± 0.03	41.3 ± 0.3

The experimental results are summarized in Table II. The high precision obtained for the direct sheet resistance ($R_0 = 63.63 \pm 0.02\ \Omega$) does not include sample variations since the measurements were performed at a single position. The low standard deviation on the Hall sheet resistance ($R_H = 0.264 \pm 0.002\ \Omega$) demonstrates the high reproducibility of M4PP measurements on p-type Ge. The calculated active Hall sheet carrier density [$N_{\mathrm{HS}} = (1.18 \pm 0.01) \times 10^{15}$ cm^{-2}] is in good agreement with the expected value considering the implanted dose. The calculated Hall mobility ($\bar{\mu}_H = 83.0 \pm 0.6$ cm^2 V^{-1} s^{-1}) is in agreement with values reported by Golikova *et al.*[26]

V. CONCLUSION

Carrier sheet concentration and mobility are key parameters with a strong effect on semiconductor device performance. Conventional measurements of these parameters become increasingly difficult with the continued miniaturization of CMOS devices, in particular for the ultrashallow junctions required; these parameters nevertheless needs to be characterized for process development and control purposes. In this work we demonstrate for the first time that M4PP's can be used to measure Hall mobility and sheet carrier concentration with little or no additional sample preparation.

The electrostatic potential due to the injected current and applied magnetic flux density is derived for an infinite sheet, a semi-infinite sheet, a narrow stripe, a quarter-plane, and a rectangle. With one or more insulating lateral boundaries present Hall effect affects the potential; without the insulating boundary only magnetoresistance is seen.

The voltage measured with a colinear, equidistant four-point probe is derived for the semi-infinite sheet and the narrow stripe sample geometries. The Hall effect contribution is separated from magnetoresistance and sheet resistance by dual configuration difference and sum methods, respectively. Finally, the sensitivity of the Hall effect signal to small angular misalignment between a four-point probe and an insulating boundary is shown to be virtually zero, which is ideal for experiments.

The theory is verified by experiments on ultrashallow implanted junctions in Si and Ge. The measured sheet carrier concentration and Hall mobility are shown to be reproducible and virtually unaffected by changes in electrode material (diamagnetic versus ferromagnetic), electrode pitch, and measurement frequency.

The microscale Hall effect measurement method has several interesting potential applications since Hall mobility and sheet carrier density may be measured (i) with high spatial resolution, (ii) without the need for lithographically defined metal contacts, (iii) on fragile samples where postpro-

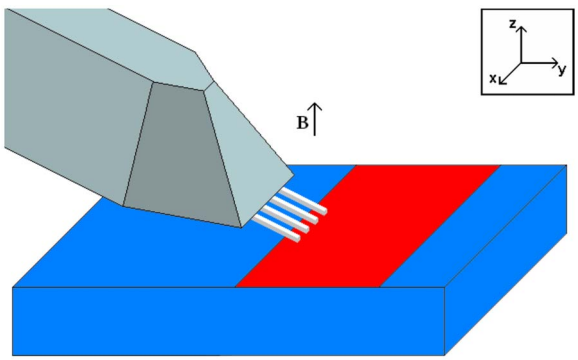

FIG. 10. (Color online) Illustration of a M4PP Hall effect measurement on a narrow stripe of highly doped Ge.

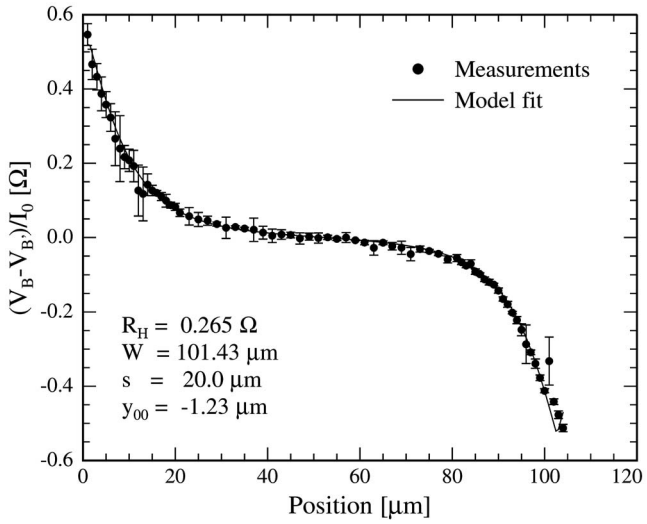

FIG. 11. Microscale Hall effect measurements on a 100 μm wide p-type Ge stripe, doped using a shallow boron implant. A line scan has been performed with a 20 μm pitch probe between the two barriers. The measurement data (●) and a fit (full line) using Eq. (22) with the Hall sheet resistance, R_H, first barrier position, y_{00}, and stripe width, w, as fitting parameters are shown.

Downloaded 08 Aug 2009 to 192.38.67.112. Redistribution subject to AIP license or copyright; see http://jap.aip.org/jap/copyright.jsp

TABLE II. Summary of measurements on the shallow *p*-type germanium junction. The sheet resistance, R_0 and the Hall sheet resistance, R_H, were measured using a 20 μm pitch M4PP, and Hall sheet carrier density, N_{HS}, and Hall mobility, $\bar{\mu}_H$, calculated using Eqs. (25) and (24).

$R_0 \pm \Delta R_0$ (Ω)	$R_H \pm \Delta R_H$ (Ω)	$N_{\mathrm{HS}} \pm \Delta N_{\mathrm{HS}}$ ($\times 10^{15}$ cm^{-2})	$\bar{\mu}_H \pm \Delta\bar{\mu}_H$ (cm^2 V^{-1} s^{-1})
63.63 ± 0.02	0.264 ± 0.002	1.18 ± 0.01	83.0 ± 0.6

cessing may alter sample properties, (iv) on micrometer sized samples, and (v) on scribe-line test structures on CMOS device wafers.

ACKNOWLEDGMENTS

The authors would like to thank Alessandra Satta and Antoine Brugere for preparation of the Ge sample. We are grateful for the financial support from Copenhagen Graduate School for Nanoscience and Nanotechnology (C:O:N:T), the Danish Research Agency (FTP). Center for Individual Nanoparticle Functionality (CINF) is sponsored by The Danish National Research Foundation. We thank Peter Bøggild for continuous support, encouragement, and fruitful discussions.

APPENDIX: QUARTER-PLANE AND RECTANGLE

Consider now the upper right quarter plane $x \geq 0$ and $y \geq 0$, see Fig. 12. The sources at $\mathbf{r}_\pm$ must be combined with ordinary images at $-\mathbf{r}_\pm$ and modified images at $\pm\bar{\mathbf{r}}_\pm$, where $\bar{\mathbf{r}}_\pm = (\bar{x}_\pm, \bar{y}_\pm) = (x_\pm, -y_\pm)$ again are the y-axis mirrored modified image positions. The potential that solves Eq. (9) in Ω is thus

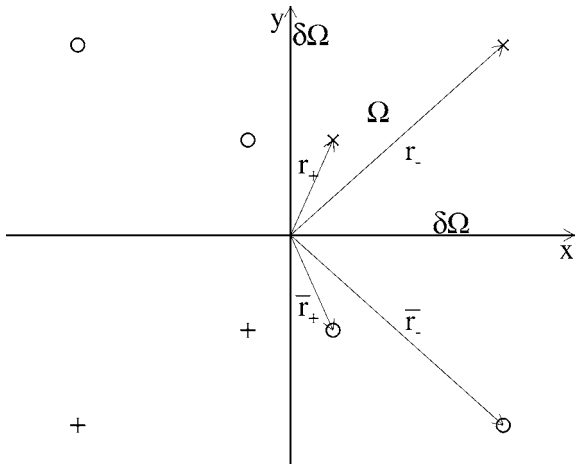

FIG. 12. Arrangement of sources ($\times$), modified images ($\bigcirc$), and ordinary images ($+$) in the upper right quarter plane case.

$$\Phi(\mathbf{r}) = \mathcal{A}_+ \ln\frac{|\mathbf{r}-\mathbf{r}_-|}{|\mathbf{r}-\mathbf{r}_+|}\frac{|\mathbf{r}+\mathbf{r}_-|}{|\mathbf{r}+\mathbf{r}_+|} + \mathcal{A}_- \ln\frac{|\mathbf{r}-\bar{\mathbf{r}}_-|}{|\mathbf{r}-\bar{\mathbf{r}}_+|}\frac{|\mathbf{r}+\bar{\mathbf{r}}_-|}{|\mathbf{r}+\bar{\mathbf{r}}_+|} + \frac{I_0 R_H}{\pi}\left(\arctan\frac{x-x_+}{y+y_+} - \arctan\frac{x-x_-}{y+y_-}\right) - \frac{I_0 R_H}{\pi}\left(\arctan\frac{y-y_+}{x+x_+} - \arctan\frac{y-y_-}{x+x_-}\right). \tag{A1}$$

Here the first term is due to the sources at $\mathbf{r}_\pm$ and the ordinary images at $-\mathbf{r}_\pm$, while the remaining three terms are due to the modified images at $\pm\bar{\mathbf{r}}_\pm$.

The potential in the rectangle, $0 \leq y \leq w$, $0 \leq x \leq \ell$, with insulating boundaries at $y=0$, $y=w$, $x=0$, and $x=\ell$ can be found from a double infinite sum of alternating modified and ordinary images. The sources and ordinary images are positioned at $\pm\mathbf{r}_\pm + 2(n\mathbf{w}+m\boldsymbol{\ell})$, while the modified images are positioned at $\pm\bar{\mathbf{r}}_\pm + 2(n\mathbf{w}+m\boldsymbol{\ell})$, where n and m are arbitrary integers and the vectors $\mathbf{w}=w\mathbf{e}_y$ and $\boldsymbol{\ell}=\ell\mathbf{e}_x$. The potential that solves Eq. (9) in Ω is thus

$$\Phi(\mathbf{r}) = \mathcal{A}_+ \sum_{n=-\infty}^{\infty}\sum_{m=-\infty}^{\infty} \ln\frac{|\mathbf{r}-\mathbf{r}_- - 2(n\mathbf{w}+m\boldsymbol{\ell})|}{|\mathbf{r}-\mathbf{r}_+ - 2(n\mathbf{w}+m\boldsymbol{\ell})|}\frac{|\mathbf{r}+\mathbf{r}_- - 2(n\mathbf{w}+m\boldsymbol{\ell})|}{|\mathbf{r}+\mathbf{r}_+ - 2(n\mathbf{w}+m\boldsymbol{\ell})|} + \mathcal{A}_- \sum_{n=-\infty}^{\infty}\sum_{m=-\infty}^{\infty} \ln\frac{|\mathbf{r}-\bar{\mathbf{r}}_- - 2(n\mathbf{w}+m\boldsymbol{\ell})|}{|\mathbf{r}-\bar{\mathbf{r}}_+ - 2(n\mathbf{w}+m\boldsymbol{\ell})|}\frac{|\mathbf{r}+\bar{\mathbf{r}}_- - 2(n\mathbf{w}+m\boldsymbol{\ell})|}{|\mathbf{r}+\bar{\mathbf{r}}_+ - 2(n\mathbf{w}+m\boldsymbol{\ell})|} + \frac{I_0 R_{\mathrm{H}}}{\pi}\sum_{n=-\infty}^{\infty}\sum_{m=-\infty}^{\infty}\left(\arctan\frac{x-x_+-2m\ell}{y+y_+-2nw} - \arctan\frac{x-x_--2m\ell}{y+y_--2nw}\right) - \frac{I_0 R_{\mathrm{H}}}{\pi}\sum_{n=-\infty}^{\infty}\sum_{m=-\infty}^{\infty}\left(\arctan\frac{y-y_+-2nw}{x+x_+-2m\ell} - \arctan\frac{y-y_--2nw}{x+x_--2m\ell}\right). \tag{A2}$$

Here the first term is due to the sources and ordinary images, while the remaining terms are due to the modified images.

From Eqs. (A1) or (A2) the measured voltages in configurations B and B′ and thus $\Delta V_{BB'}$ and $\overline{V_{BB'}}$ may be calculated; due to the limited space, however, we do not report these equations.

[1] D. K. Schroder, *Semiconductor Material and Device Characterization*, 3rd ed. (Wiley, Hoboken, NJ, 2006).
[2] International Technology Roadmap for Semiconductors, http://www.itrs.net.
[3] C. L. Petersen, T. M. Hansen, P. Bøggild, A. Boisen, O. Hansen, T. Hassenkam, and F. Grey, Sens. Actuators, A **96**, 53 (2002).
[4] D. H. Petersen, R. Lin, T. M. Hansen, E. Rosseel, W. Vandervorst, C. Markvardsen, D. Kjær, and P. F. Nielsen, J. Vac. Sci. Technol. B **26**, 362

Downloaded 08 Aug 2009 to 192.38.67.112. Redistribution subject to AIP license or copyright; see http://jap.aip.org/jap/copyright.jsp

(2008).
[5]T. Clarysse, A. Moussa, F. Leys, R. Loo, W. Vandervorst, M. C. Benjamin, R. J. Hillard, V. N. Faifer, M. I. Current, R. Lin, and D. H. Petersen, Mater. Res. Soc. Symp. Proc. **912**, 197 (2006).
[6]C. L. Petersen, R. Lin, D. H. Petersen, and P. F. Nielsen, 14th IEEE International Conference on Advanced Thermal Processing of Semiconductors, RTP '06, pp. 153–158 (IEEE, Danvers, 2006).
[7]T. Clarysse, W. Vandervorst, R. Lin, D. H. Petersen, and P. F. Nielsen, Nucl. Instrum. Methods Phys. Res. B **253**, 136 (2006b).
[8]T. Clarysse, P. Eyben, B. Parmentier, B. V. Daele, A. Satta, W. Vandervorst, R. Lin, D. H. Petersen, and P. F. Nielsen, International Workshop on Insight in Semiconductor Device Fabrication, Metrology and Modeling, Insight 2007, 2008, Vol. 26, p. 317.
[9]H. Ryssel and I. Ruge, *Ion Implantation* (Wiley, Chichester, 1986).
[10]E. H. Hall, Am. J. Math. **2**, 287 (1879).
[11]L. J. van der Pauw, Philips Res. Rep. **13**, 1 (1958a).
[12]L. J. van der Pauw, Philips Res. Rep. **20**, 220 (1958b).
[13]R. S. Popović, *Hall Effect Devices, Magnetic Sensors and Characterization of Semiconductors*, The Adam Hilger Series on Sensors (Adam Hilger, Bristol, 1991).
[14]K. Seeger, *Semiconductor Physics, An Introduction*, Solid-State Sciences No. 40, 5th ed. (Springer, Berlin, 1991).
[15]C. Herring, J. Appl. Phys. **31**, 1939 (1960).
[16]F. M. Smits, Bell Syst. Tech. J. **37**, 711 (1958).
[17]S. Ramo, T. V. Duzer, and J. R. Whinnery, *Fields and Waves in Communication Electronics* (Wiley, New York, 1984).
[18]P. Blood and J. W. Orton, *The Electrical Characterization of Semiconductors: Majority Carriers and Electron States*, Techniques of Physics Vol. 14 (Academic, London, 1992).
[19]L. B. Valdes, Proc. IRE **42**, 420 (1954).
[20]R. Baron, G. A. Shifrin, O. J. Marsh, and J. W. Mayer, J. Appl. Phys. **40**, 3702 (1969).
[21]D. W. Koon and C. J. Knickerbocker, Rev. Sci. Instrum. **64**, 510 (1993).
[22]http://www.capres.com.
[23]C. L. Petersen, D. Worledge, and P. R. E. Petersen, Mater. Res. Soc. Symp. Proc. **738**, 157 (2003).
[24]P. R. Bevington, *Data Reduction and Error Analysis for the Physical Sciences* (McGraw-Hill, New York, 1969).
[25]Y. Sasaki, K. Itoh, E. Inoue, S. Kishi, and T. Mitsuishi, Solid-State Electron. **31**, 5 (1988).
[26]O. A. Golikova, B. Y. Moizhes, and L. S. Stilbans, Sov. Phys. Solid State **3**, 2259 (1962).

Downloaded 08 Aug 2009 to 192.38.67.112. Redistribution subject to AIP license or copyright; see http://jap.aip.org/jap/copyright.jsp